



# Simulation of Deployment of a Flexible Solar Array

OSKAR WALLRAPP

*Munich University of Applied Sciences, D-80335 Munich, Germany;*  
*E-mail: wallrapp@fh-muenchen.de*

SIMON WIEDEMANN

*Cranfield University, College of Aeronautics, Cranfield, UK*

(Received: 1 January 2001; accepted in revised form: 12 June 2001)

**Abstract.** The deployment of a solar array is simulated three-dimensionally using the multibody program SIMPACK. The analyses are performed for 500 real-time seconds, which contain the three deployment phases, (I) jump-out, (II) steering phase and (III) deployed phase. The goal of the simulations is to check the influence of the flexibility of the solar array on the solar generator motions during these three phases against results obtained by a rigid body model simulation.

The modelling of flexible bodies is based on the widely used method of floating frame of reference formulation applying global shape functions (Ritz method). The preparation of a proper set of shape functions to represent the flexibility of the yoke and the six solar panels is one of the main objectives of this paper. For each of the components, eigenmodes and static modes for various boundary conditions are computed using the finite element program NASTRAN.

For a good convergence of the Ritz approximation with a small number of shape functions, the shape functions are selected using modal participation factors, that are computed for various load cases prior to the time simulations. The load cases are obtained, for example, by a rigid body simulation of the deployment phases. The proposed method of shape function selection using modal participation factors is demonstrated by examples.

**Key words:** flexible multibody systems, modal approach, mode selection, solar array.

## 1. Introduction

The deployment of a solar array as shown in Figure 1 is one of the critical moments for a satellite structure. Therefore, simulations are performed to gain knowledge about the various structural loads during deployment. The model presented here consists of the central body of the satellite, along with a yoke and six panels, which are connected by revolute joints and deployment mechanisms. The central body is inertially fixed.

The deployment is undertaken in three phases:

- (I) In phase one – called *jump-out* – the completely folded solar panels are freed from their fixations, and then deployment springs drive the solar generator open against the flexible cable mechanisms between the bodies. After some

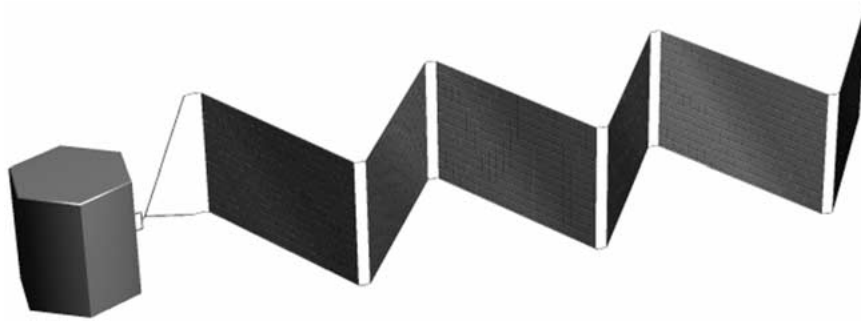


Figure 1. Scheme of the solar array of a satellite with the central body, the yoke and the six panels.

oscillations damped by various friction, a static equilibrium configuration of all the bodies and mechanisms is reached. This phase lasts 250 seconds.

- (II) In following *steering phase*, a motor gear unit controls the further deployment until all panels and the yoke lay within one plane and get locked in this position. This phase lasts 110 seconds.
- (III) In the locked and plane configuration the solar array performs a damped oscillation – *deployed phase*. The three phases take 500 real-time seconds in all.

In addition to the fast rigid body simulation, a simulation with a flexible yoke and panels is presented. The simulations are performed using the multibody program SIMPACK, which is based on an  $O(n)$  formalism and the floating frame of reference formulation [9]. As a consequence, the motion of a flexible body is a reference motion with superimposed small deformations using the Ritz method. The mode shapes and their corresponding mode shape matrices are pre-computed from results of a finite element analysis of the flexible body and are converted to the so-called standard input data (SID) [18]. The pre-processor FEMBS [19] calculates the SID for various FEM programs; the SID may also be imported by various MBS programs other than SIMPACK.

A known difficulty using the Ritz approach is the choice of proper mode shapes. The paper discusses the selection of mode shapes for various boundary conditions; the specific reference frames are referred to as Buckens frames, rigidly attached nodal frames and three-point body fixed frames. Normal vibration modes and mode shapes due to static loads (static modes) are used.

In order to reduce the computational burden and to increase the convergence of the simulation results, an efficient mode selection method is required, as is often stated in the literature. In [2, 14, 15], mode selection for multibody simulation in particular is discussed. Here, participation factors are used that are computed for various quasi-static load cases prior to time simulations.

The paper is organised as follows: Section 2 gives a brief description of the equations of motion. In Section 3, the modelling of the rigid and flexible solar array is presented. Section 4 discusses the mode selection and computation of modal participation factors and Section 5 shows the results of the simulations. The conclusion is given in Section 6.

## 2. Brief Description of Equations of Motion

A multibody system is an assembly of bodies, joints, force elements and a global reference frame with respect to which a body moves. The global reference frame is inertially fixed or accelerated. The bodies are rigid or flexible and represent the inertia of the system. Joints and force elements are massless and are attached to nodes on the surface of the bodies. They cause forces and torques at the nodes and additionally, joints yield kinematical constraint equations [8, 11].

The equations of motion of a multibody system are efficiently derived by multibody formalisms that are based on data which describe the system elements and topology. Here, the Lagrangian equations of type one are discussed. They are written as  $n_z$  redundant variables of position and velocity –  $n_z \times 1$ -matrices  $\mathbf{z}_I$  and  $\mathbf{z}_{II}$  – of the  $n$  bodies and the constraint forces –  $n_c \times 1$ -matrix  $\boldsymbol{\lambda}$  – of the  $n_G$  joints. The differential-algebraic equations (DAE) of motion in the so-called *descriptor form* with the dimension  $n_{\text{DAE}} = 2n_z + n_c$  are given as [3]

$$\left. \begin{array}{l} \dot{\mathbf{z}}_I = \mathbf{Z} \mathbf{z}_{II} \\ \mathbf{M} \dot{\mathbf{z}}_{II} - \mathbf{G}^T \boldsymbol{\lambda} = \mathbf{h}_a \\ \mathbf{g} = 0 \quad \text{or} \quad \mathbf{G} \mathbf{z}_{II} = \boldsymbol{\kappa} \end{array} \right\} \quad \text{with} \quad \mathbf{G} = \frac{\partial \mathbf{g}}{\partial \mathbf{z}_{II}}, \quad (1)$$

where  $\mathbf{Z} = \mathbf{Z}(\mathbf{z}_I)$  is the matrix of kinematic equations,  $\mathbf{M} = \mathbf{M}(\mathbf{z}_I)$  is the mass matrix,  $\mathbf{h}_a = \mathbf{h}_a(\mathbf{z}_I, \mathbf{z}_{II}, t)$  is the matrix of generalized applied forces due to stresses, gravity, body and surface forces and torques,  $\mathbf{g} = \mathbf{g}(\mathbf{z}_I, t)$  is the  $n_c \times 1$ -matrix of the implicit position constraint equations and  $\mathbf{G} = \mathbf{G}(\mathbf{z}_I, t)$  is the  $n_c \times n_z$ -constraint matrix, the Jacobian of  $\mathbf{g}$ . Matrix  $\boldsymbol{\kappa} = \boldsymbol{\kappa}(t)$  defines functions of time at joints. The matrices in (1) are the sum of matrices that describe a single body and its forces and torques (index  $i$ ) and a single joint (index  $s$ ). Thus

$$\left. \begin{array}{l} \mathbf{z}_I = [\mathbf{z}_I^i], \quad \mathbf{z}_{II} = [\mathbf{z}_{II}^i], \quad \boldsymbol{\lambda} = [\boldsymbol{\lambda}^s], \quad \mathbf{g} = [\mathbf{g}^s], \\ \mathbf{Z} = \text{diag} [\mathbf{Z}^i], \quad \mathbf{M} = \text{diag} [\mathbf{M}^i], \quad \mathbf{h}_a = [\mathbf{h}_a^i], \\ n_z = \sum_{i=1}^n n_z^i, \quad n_c = \sum_{s=1}^{n_G} n_c^s, \end{array} \right\} \quad (2)$$

where  $i = 1, \dots, n$ ,  $s = 1, \dots, n_G$ .

SIMPACK uses a topology that forms a multibody system with a tree structure and applies Equation (1) for joints, leading to kinematically closed loops. More details are given in [9].

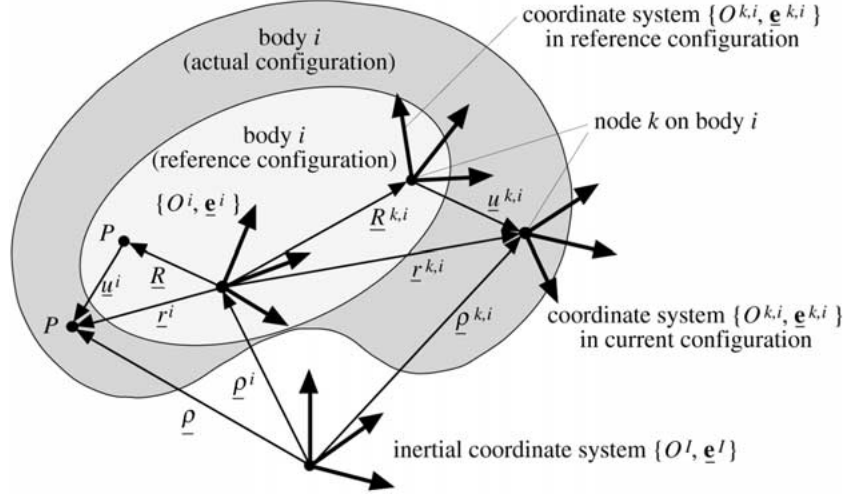


Figure 2. General model of a representative body  $i$ .

### 2.1. KINEMATICS OF A FLEXIBLE BODY

The model of a flexible body  $i$  is a continuum in general with internal constraints in particular such as beams and plates or a finite element model. Assuming that the deformations are small, a common formulation is that of a floating body reference frame  $\{O^i, \underline{e}^i\}$  and linearised equations of deformation [10]. The total motion is a (large) motion of the reference frame with respect to the global (inertial) frame  $\{O^I, \underline{e}^I\}$  and small deformations with respect to the reference frame.  $O^I$  and  $O^i$  denote the origin,  $\underline{e}^I$  and  $\underline{e}^i$  the Cartesian basis of the coordinate frames. It is noted that all vectors in Figure 2 and in the following figures are represented by coordinates with respect to the basis  $\underline{e}^i$ .

The rotation of the body reference frame is given by  $\alpha^i(t)$  and  $\omega^i(t)$ , the translation by  $\rho^i(t)$  and  $\mathbf{v}^i(t)$ , thus yielding the location and velocity of the body with respect to the global frame, see Figure 2. The corresponding kinematic equations are

$$\begin{aligned} \underline{e}^i &= \mathbf{A}^i \underline{e}^I \quad \text{where} \quad \mathbf{A}^i = \mathbf{A}^i(\alpha^i), \\ \tilde{\omega}^i &= \mathbf{A}^i \dot{\mathbf{A}}^{iT} \quad \text{or} \quad \dot{\alpha}^i = \mathbf{Z}_r^i \omega^i, \quad \dot{\rho}^i = \mathbf{v}^i + \tilde{\omega}^i \omega^i, \end{aligned} \quad (3)$$

where  $\mathbf{Z}_r^i$  is a  $3 \times 3$ -matrix, relating the angular velocity coordinates  $\omega^i$  with the time derivatives of the angles  $\alpha^i$ . In the reference configuration the position of all material points  $P$  with respect to the reference frame is given by  $\mathbf{R}$ . Models with internal constraints such as beams use rigid parts of the body that rotate. Their orientation is defined introducing a frame  $\{P, \underline{e}\}$  at  $P$  and is measured by the rotation matrix  $\Gamma^i = \Gamma^i(\mathbf{R})$  satisfying  $\underline{e} = \Gamma^i \underline{e}^i$ . In the reference configuration matrix  $\Gamma^i$  is mostly given by an identity matrix  $\mathbf{E}$ . In the actual configuration, the

points  $P$  are inertially described by position  $\rho(\mathbf{R}, t)$  and orientation  $\mathbf{A}(\mathbf{R}, t)$ . The velocities are  $\mathbf{v}(\mathbf{R}, t)$  and  $\omega(\mathbf{R}, t)$  for translation and rotation, respectively.

As shown in Figure 2, vectors  $\mathbf{u}^i(\mathbf{R}, t)$  and  $\boldsymbol{\vartheta}^i(\mathbf{R}, t)$  are introduced for translational and rotational deformation, respectively. Thus

$$\begin{aligned}\rho &= \rho^i + \mathbf{r}^i, \quad \mathbf{r}^i = \mathbf{R} + \mathbf{u}^i, \quad \mathbf{v} = \mathbf{v}^i + \dot{\mathbf{r}}^i + \tilde{\omega}^i \mathbf{r}^i, \quad \dot{\mathbf{r}}^i = \dot{\mathbf{u}}^i, \\ \underline{\mathbf{e}} &= \mathbf{A} \underline{\mathbf{e}}^i, \quad \mathbf{A} \stackrel{\text{lin}}{=} (\mathbf{E} - \tilde{\boldsymbol{\vartheta}}^i) \Gamma^i \mathbf{A}^i(\alpha^i), \quad \omega \stackrel{\text{lin}}{=} \omega^i + \dot{\boldsymbol{\vartheta}}^i.\end{aligned}\quad (4)$$

For  $\mathbf{u}^i(\mathbf{R}, t)$  and  $\boldsymbol{\vartheta}^i * \mathbf{R}, t$ , a Ritz approximation

$$\left. \begin{aligned} \mathbf{u}^i(\mathbf{R}, t) &= \Phi^i(\mathbf{R}) \mathbf{q}^i(t), \quad \Phi^i = [\phi_{\alpha l}^i] \\ \boldsymbol{\vartheta}^i(\mathbf{R}, t) &= \Psi^i(\mathbf{R}) \mathbf{q}^i(t), \quad \Psi^i = [\psi_{\alpha l}^i] \end{aligned} \right\}, \quad \mathbf{q}^i(t) = [q_l^i(t)], \quad \begin{aligned} l &= 1, 2, \dots, n_q^i, \\ \alpha &\triangleq x, y, z, \end{aligned} \quad (5)$$

is used where  $\Phi^i(\mathbf{R})$  and  $\Psi^i(\mathbf{R})$  are shape functions (mode shapes) and  $\mathbf{q}^i(t)$  unknown time functions.  $n_q^i$  is the number of shape functions. Therefore, the variables in (2) to represent position and velocity of a body  $i$  and its kinematic matrix are

$$\mathbf{z}_l^i = \begin{bmatrix} \rho^i \\ \alpha^i \\ \mathbf{q}^i \end{bmatrix}, \quad \mathbf{z}_{lI}^i = \begin{bmatrix} \mathbf{v}^i \\ \omega^i \\ \dot{\mathbf{q}}^i \end{bmatrix}, \quad \mathbf{Z}^i = \begin{bmatrix} \mathbf{E} & \tilde{\rho}^i & \mathbf{0} \\ \mathbf{0} & \mathbf{Z}_r^i & \mathbf{0} \\ \mathbf{0} & \mathbf{0} & \mathbf{E} \end{bmatrix}, \quad (6)$$

where  $n_z^i = 6 + n_q^i$  is the number of position variables of body  $i$ . Substituting  $\mathbf{R}$  by  $\mathbf{R}^{k,i}$ , Equations (4) and (5) describe the motion of a single node  $k$  of body  $i$  and its frame  $\{O^{k,i}, \underline{\mathbf{e}}^{k,i}\}$  as shown in Figure 2.

## 2.2. CONDITIONS OF SHAPE FUNCTIONS AND CONSTRAINTS

Convergence of the Ritz method in (5) towards the solution of the partial differential equation describing body deformation is assured if the shape functions form a complete set of functions and if they satisfy the geometrical boundary conditions [1]. Note that the convergence of the solution is not monotonic even if the shape functions satisfy the dynamical boundary conditions. Such functions are called *admissible functions* [6]. The expansion theorem defines the conditions, under which *eigenfunctions* or *eigenmodes* form a complete set of admissible functions. Using eigenfunctions violating the dynamical boundary conditions, the convergence of the Ritz method is often poor, especially when evaluating the internal forces of a flexible body. Convergence can be improved significantly by introducing an expanded class of admissible functions, called *quasi-comparison functions* [4, 5]. These are functions that fulfil dynamical boundary conditions (at least a linear combination of these functions). In practice, the use of shape functions for static load cases (*static modes*) increase the convergence considerably in addition to eigenmodes. In multibody dynamics the boundary conditions are often unknown, therefore researchers use sets of mode shapes that may violate the geometrical boundary conditions. In this case the boundary conditions must be satisfied using

the deformation coordinates  $\mathbf{q}^i(t)$  in (5) yielding a slower convergence towards the real solution.

The variables  $\mathbf{z}_I, \mathbf{z}_{II}$  are not independent. Three types of constraints are considered:

- (a) The constraints of a specific model describe the internal body motions, e.g. the motion of rigid cross sections for the Bernoulli beam.
- (b) In (4) twelve variables  $\rho^i(t), \alpha^i(t), \mathbf{u}^i(\mathbf{R}, t)$  and  $\vartheta^i(\mathbf{R}, t)$  define the motion of the coordinate frame  $\{P, \underline{\mathbf{e}}\}$ . Thus to be able to compute the six position and orientation variables of the body reference frame six additional constraints are necessary. They can efficiently be defined by choosing mode shapes that satisfy the geometrical boundary conditions *a priori*.
- (c) Joints between nodes of the bodies and of the global frame lead to constraint equations depending on  $\mathbf{z}_I$  and time  $t$ .

By considering the selected shape functions  $\Phi^i(\mathbf{R})$  and  $\Psi^i(\mathbf{R})$  of a flexible body introduced in (5), the constraints of type (a) are satisfied automatically. For the constraints defined in (b) the following bodyreference frames are frequently used:

- (i) *Tangent* or node fixed frame at node  $\mathbf{R} = \mathbf{R}^{Fi}$  yields  $O^i = P(\mathbf{R} = \mathbf{R}^{Fi})$  and  $\underline{\mathbf{e}}^i \equiv \underline{\mathbf{e}}(\mathbf{R} = \mathbf{R}^{Fi})$  and thus applying (5)

$$\mathbf{u}^i(\mathbf{R}^{Fi}, t) = \Phi^i(\mathbf{R}^{Fi})\mathbf{q}^i(t) = \mathbf{0} \quad \text{and} \quad \vartheta^i(\mathbf{R}^{Fi}, t) = \Psi^i(\mathbf{R}^{Fi})\mathbf{q}^i(t) = \mathbf{0}. \quad (7)$$

- (ii) Frame, which is based on three body nodes  $\mathbf{R}^{Fi}, \mathbf{R}^2$ , and  $\mathbf{R}^3$  and so-called *chord* frame. The origin is given by  $O^i = P(\mathbf{R} = \mathbf{R}^{Fi})$ , the basis  $\underline{\mathbf{e}}^i$  is oriented in the planes expressed by the three nodes. This yields the following six conditions

$$\begin{aligned} \mathbf{u}^i(\mathbf{R}^1, t) &= \Phi^i(\mathbf{R}^{Fi})\mathbf{q}^i(t) = \mathbf{0}, & u_2^i(\mathbf{R}^2, t) &= \Phi_{2*}^i(\mathbf{R}^2)\mathbf{q}^i(t) = 0, \\ u_3^i(\mathbf{R}^2, t) &= \Phi_{3*}^i(\mathbf{R}^2)\mathbf{q}^i(t) = 0, & u_3^i(\mathbf{R}^3, t) &= \Phi_{3*}^i(\mathbf{R}^3)\mathbf{q}^i(t) = 0. \end{aligned} \quad (8)$$

- (iii) *Tisserand* or mean-axis frame at the center of mass  $CM^i$  of the deformed body and its basis  $\underline{\mathbf{e}}^i$  rotates so that the relative angular momentum  $\mathbf{H}_{\text{rel}}^i = \mathbf{0}$ . In addition to  $\mathbf{R}_{CM}^i = \mathbf{0}$ , these definitions imply that the relative linear momentum  $\mathbf{J}_{\text{rel}}^i = \mathbf{0}$ .  $\mathbf{J}_{\text{rel}}^i$  and  $\mathbf{H}_{\text{rel}}^i$  are given by

$$\mathbf{J}_{\text{rel}}^i = \int_{V_0^i} \dot{\mathbf{u}}^i dm = \mathbf{C}_t^i \dot{\mathbf{q}}^i = \mathbf{0},$$

$$\begin{aligned} \mathbf{H}_{\text{rel}}^i &= \int_{V_0^i} (\tilde{\mathbf{R}} + \tilde{\mathbf{u}}) \dot{\mathbf{u}}^i dm = (\mathbf{C}_{r0}^i + \mathbf{C}_{r1}^i(\mathbf{q}^i)) \dot{\mathbf{q}}^i = \mathbf{0}, \quad \text{and} \\ \mathbf{C}_t^i &= \int_{V_0^i} \Phi^i dm, \quad \mathbf{C}_{r0}^i = \int_{V_0^i} \tilde{\mathbf{R}} \Phi^i dm, \quad \mathbf{C}_{r1}^i = \int_{V_0^i} (\Phi^i \mathbf{q}^i)^\sim \Phi^i dm. \end{aligned} \quad (9)$$

In (9)  $V_0^i$  is the body volume and  $dm$  is the mass increment. A linearised form of (9), the *Buckens* frame, only takes into account matrices  $\mathbf{C}_t^i$  and  $\mathbf{C}_{r0}^i$ .

The six constraint equations due to the reference given in (7) to (9) can be satisfied *a priori* by using corresponding boundary conditions for the shape functions. This is illustrated by the following examples: The mode shapes of a structure, which is clamped at node  $\mathbf{R}^{Fi}$  satisfy (7) because  $\Phi^i(\mathbf{R}^{Fi}) = \mathbf{0}$  and  $\Psi^i(\mathbf{R}^{Fi}) = \mathbf{0}$ . The chord frame is applied by using mode shapes of a simple supported beam of length  $\ell^i$ , where  $\Phi^i(\mathbf{R}^{Fi}) = \mathbf{0}$  and  $\Phi_{2*}^i(R_1^2 = \ell^i) = 0$ . The Buckens frame is applied if mode shapes of an unsupported structure are used without the rigid body modes, because the integrals in (9) yield zero matrices for  $\mathbf{C}_t^i$  and  $\mathbf{C}_{r0}^i$ . If in addition  $\mathbf{C}_{r1}^i = \mathbf{0}$ , a Tisserand frame is obtained. Using such a specific body reference frame, the mode shapes must be transformed accordingly to satisfy the geometrical boundary conditions, [12], prior to insertion into the equations of motion.

The last type of constraint is related to joints and leads to restricted motions of the two connected nodes with respect to each other. Assuming that a joint  $s$  is defined from node  $l$  of body  $j$  to node  $k$  of body  $i$  the relative position and orientation are given by

$$\begin{aligned} \underline{d}^s &= \underline{\rho}^{k,i} - \underline{\rho}^{l,j} = \underline{\mathbf{e}}^{k,i} \mathbf{d}^s, \\ \mathbf{B}^s &= \mathbf{B}^s(\boldsymbol{\beta}^s) = \mathbf{A}^{k,i} \mathbf{A}^{k,i} \mathbf{A}^{l,jT} \quad \text{for} \quad \underline{\mathbf{e}}^{k,i} = \mathbf{B}^s \underline{\mathbf{e}}^{l,j}. \end{aligned} \quad (10)$$

The relative motion given by the matrices  $\mathbf{d}^s = [d_\alpha^s]$  and  $\boldsymbol{\beta}^s = [\beta_\alpha^s]$  can be expressed by (4) to (6) in terms of the system variables  $\mathbf{z}_I$ , and in case of excitations also in terms of time  $t$ . A joint  $s$  restricts  $0 \leq n_c^s \leq 6$  motions of the relative variables  $\mathbf{d}^s$  and  $\boldsymbol{\beta}^s$  and their time derivatives and may be written in accordance with (2) as

$$\mathbf{g}^s(\mathbf{z}_I, t) = \mathbf{0} \quad \text{and} \quad \mathbf{G}^s(\mathbf{z}_I, t) \mathbf{z}_{II} = \boldsymbol{\kappa}(t). \quad (11)$$

Equation (11) defines holonomic constraint equations for the variables describing the body reference motion and the deformation [8]. In SIMPACK mode shapes must *a priori* satisfy conditions of type (a) and (b). Constraints referring to (c) will be considered by the use of generalized coordinates  $\mathbf{z}_I$  in the tree structure of the multibody system and additional closed loop constraints in the form of (11) yielding the DAEs as shown in (1).

### 2.3. DYNAMICS OF A FLEXIBLE BODY

Referring to the assumptions of the flexible body model as defined before, inertia forces, stresses, body forces  $\mathbf{k}_0^i(\mathbf{R}, t)$  due to gravity, surface forces  $\bar{\mathbf{p}}_0^i(\mathbf{R}, t)$ , forces  $\mathbf{F}^{k,i}$ , torques  $\mathbf{L}^{k,i}$  due to force elements (subscript  $f$ ), and joints (subscript  $c$ ) at nodes  $k, i$  are considered.

The virtual power of these forces acting on  $n$  bodies in terms of the generalised velocities  $\mathbf{z}_{II}^i$  as defined in (2) is

$$\delta P = \sum_{i=1}^n \delta \mathbf{z}_{II}^i{}^T (\mathbf{M}^i \dot{\mathbf{z}}_{II}^i - \mathbf{h}_a^i - \mathbf{h}_c^i)$$

with  $\mathbf{h}_a^i = \mathbf{h}_\omega^i + \mathbf{h}_g^i + \mathbf{h}_e^i + \mathbf{h}_p^i + \mathbf{h}_f^i.$  (12)

In (12) matrix  $\delta \mathbf{z}_{II}^i$  denotes the virtual velocity of  $\mathbf{z}_{II}^i$  and  $\mathbf{M}^i$ ,  $\mathbf{h}_a^i$  and  $\mathbf{h}_c^i$  denote the corresponding generalised masses, applied forces and constraint forces. As shown in (12) matrix  $\mathbf{h}_a^i$  is the sum of generalized applied forces such as the inertia forces  $\mathbf{h}_\omega^i$  due to the angular velocity  $\boldsymbol{\omega}^i$  in (3), the gravitational forces  $\mathbf{h}_g^i$  due to  $\mathbf{k}_0^i(\mathbf{R}, t)$ , the internal forces  $\mathbf{h}_e^i$  due to body deformations, the surface forces  $\mathbf{h}_p^i$  due to  $\bar{\mathbf{p}}_0^i(\mathbf{R}, t)$  and forces  $\mathbf{h}_f$  arising from the nodal forces  $\mathbf{F}_f^{k,i}$  and torques  $\mathbf{L}_f^{k,i}$  due to force elements. Similarly,  $\mathbf{h}_c^i$  is given by nodal constraint forces  $\mathbf{F}_c^{k,i}$  and torques  $\mathbf{L}_c^{k,i}$  due to joints. Since  $\delta \mathbf{z}_{II}^i$  depends on constraints of type (c), given in (11), matrix  $\mathbf{h}_c^i$  can be expressed in terms of the constraint matrix  $\mathbf{G}^s$  and the Lagrange multipliers  $\boldsymbol{\lambda}^s$ . With (11) and (12) the equations of motion given in (1) and (2) are derived. All generalised forces and masses in (12) are algebraic expressions containing the variables (6) and integrals of the functions  $\boldsymbol{\Phi}^i(\mathbf{R})$  and  $\boldsymbol{\Psi}^i(\mathbf{R})$ , see [11, 18].

Matrices  $\mathbf{M}^i$ ,  $\mathbf{h}_e^i$ , and  $\mathbf{h}_f^i = \sum \mathbf{h}_n^{k,i}$  of all applied nodal forces and torques acting on body  $i$  are shown in detail as follows. Partitioning these matrices in the same way as matrix  $\mathbf{z}_{II}^i$  in (6) yields [11, 18]

$$\mathbf{M}^i = \begin{bmatrix} m^i \mathbf{E} & \text{sym} \\ m^i \tilde{\mathbf{c}}^i & \mathbf{I}^i \\ \mathbf{C}_t^i & \mathbf{C}_r^i & \mathbf{M}_e^i \end{bmatrix}, \quad \mathbf{h}_e^i = \begin{bmatrix} \mathbf{0} \\ \mathbf{0} \\ -(\mathbf{K}_e^i + \mathbf{K}_{\text{geo}}^i) \mathbf{q}^i - \mathbf{D}_e^i \dot{\mathbf{q}}^i \end{bmatrix},$$

$$\mathbf{h}_n^{k,i} = \begin{bmatrix} \mathbf{F}^{k,i} \\ \tilde{\mathbf{r}}^{k,i} \mathbf{F}^{k,i} + \mathbf{L}^{k,i} \\ \boldsymbol{\Phi}^{k,iT} \mathbf{F}^{k,i} + \boldsymbol{\Psi}^{k,iT} \mathbf{L}^{k,i} \end{bmatrix}. \quad (13)$$

Indices  $t$ ,  $r$  and  $e$  denote the translation and rotation of the reference motion and the elastic deformation, respectively. Symbol  $m^i$  in (13) denotes the mass of body  $i$ .  $\mathbf{I}^i$  and  $\mathbf{c}^i$  are the inertia matrix and the position matrix of the center of mass  $CM^i$  of the deformed body with respect to the origin  $O^i$ . Sub-matrix  $\mathbf{M}_e^i$  contains the generalised masses corresponding to the velocities  $\dot{\mathbf{q}}^i$ , while  $\mathbf{C}_t^i$  and  $\mathbf{C}_r^i$  are matrices



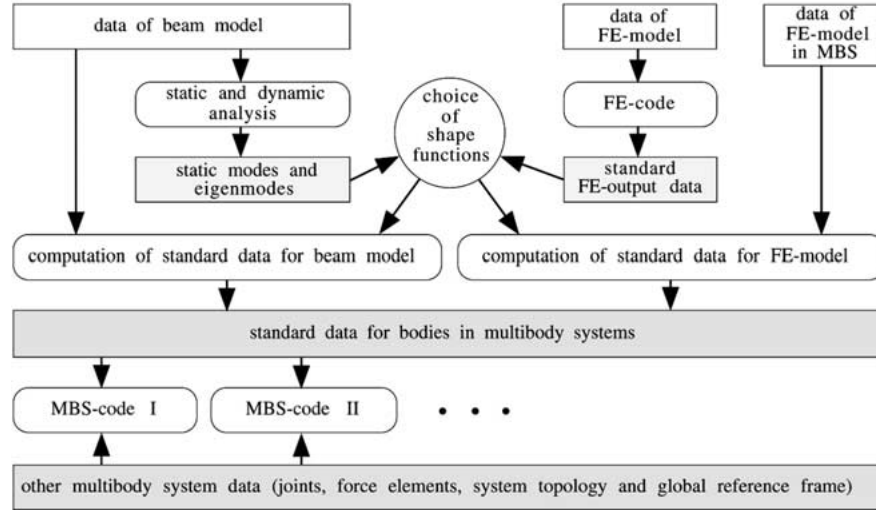


Figure 3. Multibody system data and pre-processors for computation of body data.

representing coupling effects between reference motion and deformation already defined in (9).  $\mathbf{K}_e^i$  is the generalized linear stiffness matrix of deformation and  $\mathbf{K}_{\text{geo}}^i$  takes geometrical non-linearities due to large forces into account.  $\mathbf{D}_e^i$  represents damping of the structure. Matrix  $\mathbf{h}_n^{k,i}$  denotes the result of generalized nodal forces and torques at node  $k, i$ , where  $\mathbf{r}^{k,i}$  is the position vector of the node defined in (4) if  $\mathbf{R} = \mathbf{R}^{k,i}$ .

The submatrices in (13) are algebraic expressions in terms of integrals of the functions  $\Phi^i(\mathbf{R})$  and  $\Psi^i(\mathbf{R})$  and can be pre-calculated before time simulation [11, 18].

#### 2.4. MULTIBODY SYSTEM DATA

The equations of motion, as derived above, imply the definition of data to describe a multibody system. These may be separated into data representing bodies, joints, force elements, the motion of the global reference frame and the system topology. All this is extensively discussed in the literature on dynamics of rigid body systems. In [7] an object oriented data model is proposed for such systems. It is extended by a set of standard input data describing flexible bodies in multibody systems [18]. The definition of these data is based on Equations (12) and (13), where the shape functions  $\Phi^i(\mathbf{R})$  and  $\Psi^i(\mathbf{R})$  are required.

As previously mentioned, eigenmodes and static modes of flexible body models, such as beams, plates and finite element structures provide a set of shape functions describing the deformation of the body approximately. The pre-processors BEAM [17] and FEMBS [19] have been developed to compute all input data of a flexible body  $i$  based on beam and finite element models, respectively. Using structural

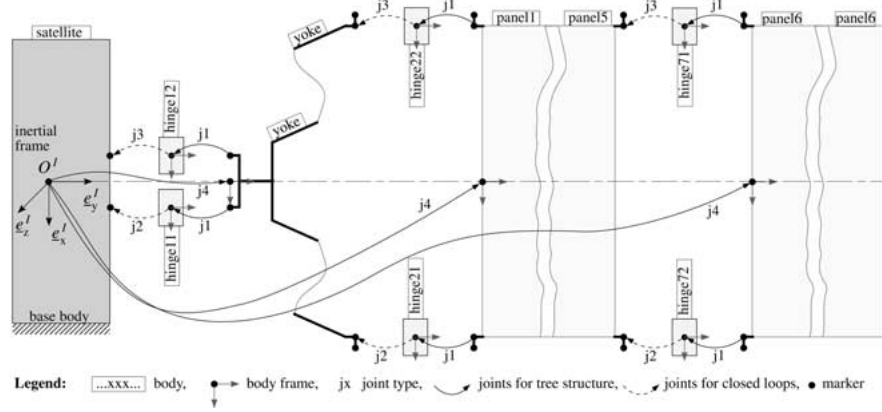


Figure 4. Topology of the solar array showing the tree structure and the closed loops.

data of a beam model, BEAM computes the eigenmodes and the standard data after mode selection. FEMBS inputs are mass, stiffness and mode shape matrices, as well as static modes of a finite element structure. The output is the standard data for a specific choice of modes. The flow of data is shown in Figure 3 and more details are given in [11].

### 3. Modelling of the Satellite

#### 3.1. TOPOLOGY OF THE MULTIBODY SYSTEM

The model consists of the central body, the yoke, and six panels. The central body is inertially fixed; while the yoke and panels are modelled as rigid or flexible bodies, that in reality are attached to each other by two pins (Figure 1). Therefore, in the case of a rigid body model, specific joints have to be used to describe the motion of the yoke and the six panels in a total of  $n_f = 7$  degrees of freedom (DOFs). As shown in Figure 4, every pin is modelled by an approximately massless rigid body called hinge that is attached by a revolute joint (denoted joint type  $j1$ ) on the right hand side. To satisfy the Gruebler condition every hinge at the bottom has a universal joint (denoted joint type  $j2$ ) to the left hand side, whereas a hinge at the top has a universal joint with an additional free motion in the  $x$ -direction (marked as joint type  $j3$ ) to the left hand side. Counting the number of all bodies  $n$  and all joints  $n_G$ , as shown in Figure 4, yields for the rigid body model as

$$n_f = 6n - \sum_{s=1}^{n_G} n_c^s = 7 \quad \text{for} \quad \begin{cases} n = 21, \\ n_G = 28, \end{cases}$$

$$n_c^s = \begin{cases} 5 \text{ for joint type } j1 \ (d_x^s = d_y^s = d_z^s = \beta_y^s = \beta_z^s = 0) \\ 4 \text{ for joint type } j2 \ (d_x^s = d_y^s = d_z^s = \beta_x^s = 0) \\ 3 \text{ for joint type } j3 \ (d_y^s = d_z^s = \beta_x^s = 0). \end{cases} \quad (14)$$

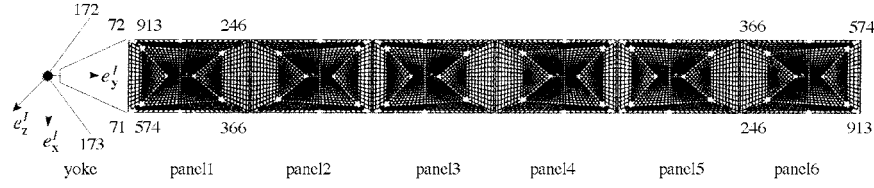


Figure 5. Finite element structure of the solar array including numbers of important nodes.

In (14) the constraint equations of joint  $j1$ ,  $j2$ , and  $j3$  are described in terms of the relative joint position and orientation given in (10). In the case of flexible bodies, the number of DOFs is given by seven plus the sum of the number of shape functions  $n_q^i$  of each body  $i$ .

To vary the type of the floating frame of reference shown in Section 2.2 an over-determined multibody system is used. Thus the body reference frame of the yoke and each of the six panels has six DOFs w. r. t. the base body denoted by a joint  $j4$  in Figure 4. Finally, the number of the coordinates is given by the DOFs of all joints of type  $j4$  and  $j1$ . This describes the tree structure of the multibody system. The number of the additional (closed loop) constraints  $n_c$  is given by the joints  $j2$  and  $j3$ , and for the satellite model we find

$$n_z = 7 \cdot 6 + 14 \cdot 1 + \sum_{i=1}^n n_q^i = 56 + \sum_{i=1}^n n_q^i, \quad n_c = 7 \cdot (4 + 3) = 49.$$

$$\text{for } n_f = n_z - n_c \quad \text{and} \quad n_{\text{DAE}} = 2 n_z + n_c. \quad (15)$$

As an alternative to the constraints due to the joints  $j2$  and  $j3$ , flexible spatial coupling elements with high stiffness can be used, but that leads to excessive numerical burdens.

### 3.2. MODELS OF THE YOKE AND PANELS

Basically, the yoke and panels are modelled using the finite element code NAS-TRAN (Figure 5). The yoke and the six identical panels are represented by thin beam and plate structures. The yoke is 2.432 m long, while the panels are 3.610 m long, and the corresponding masses are 6.66 and 21.95 kg, respectively. Since FEMBS is restricted with respect to the DOFs of a single body, a nodal reduction to 69 nodes is applied to the panels.

The creation of standard body data for (1), (2), and (13) requires the definition of the reference frame and its corresponding boundary conditions, the computation of mode shapes and the calculations in FEMBS. Three cases of reference frames are discussed for the yoke and the panel in the following:

1. Buckens frame for a free body, yielding  $\mathbf{C}_t^i = \mathbf{C}_{r0}^i = \mathbf{0}$  in (9) and six rigid body modes.

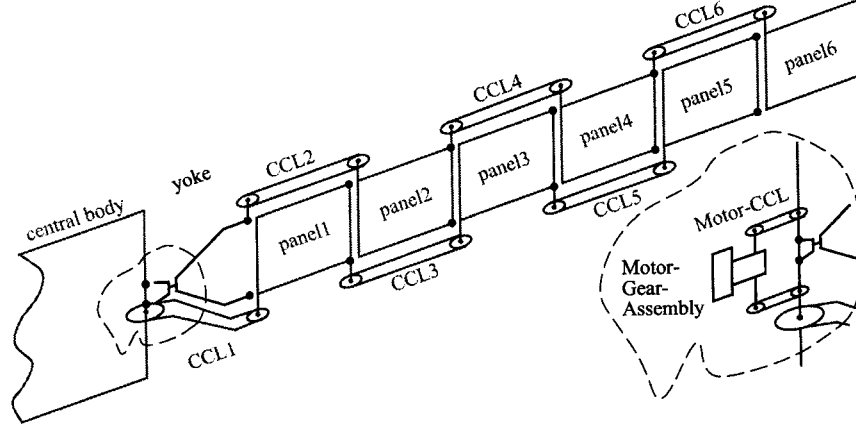


Figure 6. Position of the force elements representing the deployment mechanisms. Every • marks the position of a hinge with a revolute joint, a deployment spring and a lock mechanism.

2. Buckens frame for a yoke supported by spherical joints at nodes 172 and 173 (panels at nodes 915 and 574 or 366 and 246), yielding  $\mathbf{C}_{r0}^i = \mathbf{0}$  in (9) and one rigid body mode.
3. Chord frame for a yoke supported as defined in (ii), Section 2.2, and constrained by  $d_z^s = 0$  at node 72, see (8). The panels are supported in a similar way.

According to these boundary conditions, natural frequencies are computed as listed in Table I. Additionally, five static modes for the yoke are prepared for loads at node 71 and node 72 and boundary conditions as given in case 2), where the free rotation is locked at node 173. The loads are a force in  $x$ ,  $y$  and  $z$  at node 71, a force in  $z$  and a torque about  $x$  at node 72.

### 3.3. MODELS OF DEPLOYMENT MECHANISMS

During the deployment defined in Section 1, different force elements control the motions of the various bodies, i.e. the yoke and panels. The deployment springs provide the energy to move the yoke and the panels; the lock mechanisms fix the bodies in the proper positions; while the closed cable loops (CCL) harmonise the movement of the yoke and panels. Finally, a motor gear unit controls the rotation of the yoke with respect to the central body by two CCLs, (the motor unit with the two CCLs is called the Motor-CCL). Figure 6 shows the position of all the force elements that are subsequently described in detail.

*Deployment springs* are attached to every hinge. Every spring provides the deployment with a constant torque  $L_0 = 1$  Nm. The springs work from the folded

Table I. Natural vibration frequencies of the yoke and the panel applying cases of reference frame: (1) = free structure, (2) = rotating structure and (3) = simple supported structure. The modes marked by • are taken for simulations in Section 5, where  $B$  denotes bending and  $T$  torsion.

	<i>Body</i> ⇒	<b>Yoke</b>			<b>Panel</b>		
	<i>Case</i> ⇒	1)	2)	3)	1)	2)	3)
Mode and frequen. in Hz ⇒	1	B • 32.75	B • 3.584	B • 3.58	T • 3.97	T • 2.23	T • 2.23
	2	T • 33.23	T • 6.047	T • 4.05	B • 9.54	B • 6.77	B • 4.23
	3	• 36.66	• 15.921	• 14.26	• 14.13	• 11.18	• 11.18
	4	• 44.63	• 37.502	• 31.99	• 21.71	• 17.90	• 11.52
	5	• 60.60	• 39.249	37.53	• 23.20	• 21.82	• 18.50
	6	• 72.37	• 39.840	39.84	27.96	• 27.88	23.11
	7	• 99.95	• 57.147	• 51.23	• 31.65	• 28.38	• 28.38
	8	• 110.58	• 63.098	63.09	• 33.13	29.31	• 29.01
	9	139.25	• 73.156	73.05	47.93	44.39	37.63
	10	157.04	• 107.56	• 96.86	48.93	44.55	44.55
	11	199.53	110.39	110.37	• 57.51	48.91	46.91
	12	• 207.67	140.24	• 138.63	62.69	• 54.84	• 54.84
	13	• 220.46	• 156.38	140.25	67.70	62.02	62.01
	14	279.83	215.31	• 191.48	76.65	67.13	62.42
	15	297.94	221.99	221.88	78.67	72.11	67.13
	16	319.67	277.87	• 242.63	79.16	77.60	74.96
	17	• 383.61	318.88	279.48	86.94	78.00	77.98
	18	389.10	• 381.77	• 331.63	105.95	80.42	80.42
	19	423.55	388.89	387.02	106.75	103.73	91.14
	20	520.55	423.28	390.58	109.02	105.10	105.06
	21	• 563.98	• 504.99	• 436.69	111.29	107.31	106.70
	22	577.76	534.08	508.96	114.67	108.75	108.54
	23	578.08	575.76	• 537.20	125.70	110.49	110.02
	24	• 607.04	577.51	575.91	140.12	123.45	120.68
	25	• 708.82	• 603.23	• 597.74	142.25	132.26	123.59
	26	739.74	611.15	605.46	150.52	133.97	132.26
	27	782.33	• 708.80	611.16	151.44	140.87	134.17
	28	• 869.67	740.25	• 732.43	169.96	143.80	143.76
	29	885.99	790.51	789.64	177.65	146.62	146.61
	30	921.12	869.48	• 866.65	180.54	153.38	149.35

position, such that the yoke is driven away from the central body, panel1 from the yoke, panel2 from panel1, etc.

Joint friction is assumed to be modelled as a linear torsional viscose damper (factor  $D_D$ ) to damp out transient oscillations of the solar array. With  $\dot{\beta}$  being the relative angular velocity of the corresponding joint, the always present total torque  $L_D$  is thus

$$L_D = L_0 + D_D \dot{\beta}. \quad (16)$$

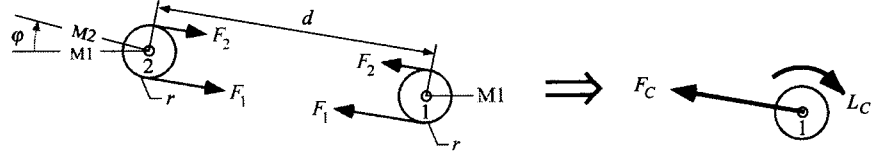


Figure 7. Cable forces  $F_1$  and  $F_2$  of CCL for stretched cables leading to forces and torques  $F_C$  and  $L_C$ .

*Lock mechanisms* are positioned on every hinge, like the deployment springs. They are activated if angle  $\beta$  of a revolute joint is equal to the lock angle  $\beta_0$  for the first time. Lock mechanisms are also damped (factor  $D_L$ ). With the stiffness  $k_L$  the torque law is

$$\begin{aligned} L_L &= 0, & \text{if mechanism is not active,} \\ L_L &= (\beta - \beta_0)k_L + \dot{\beta}D_L, & \text{if mechanism is active.} \end{aligned} \quad (17)$$

The exact computation of (17) is proven to be crucial for correct results. In SIM-PACK accuracy is guaranteed using so-called root-functions.

*Closed cable loops* (CCL) connect the central body with panel1, the yoke with panel2, panel1 with panel3, etc. (Figure 6). Their function is to keep the linked bodies parallel to each other, except for CCL1. A CCL consists of two pulleys linked by a cable loop. If the two bodies linked by a CCL are not parallel, but distorted by an angle  $\varphi$  as shown in Figure 7, the different cable forces produce a corrective torque  $L_C$ . Angle  $\varphi$  denotes the relative rotation of two pulleys and can be measured using the lines M1 and M2 that are parallel in the initial configuration. Since the cable forces are always parallel to an imaginary line connecting the two pulley centres, always coincides with this imaginary line. With a cable stiffness  $k_C$ , a pre-tension  $F_0$ , the change of distance between the pulley centres  $d-d_0$ , pulley radius  $r$  and distortion angle  $\varphi$  the force laws are

$$\left. \begin{aligned} F_1 &= F_0 + (d - d_0)k_C + \varphi r k_C & \text{with } F_1 \geq 0, \\ F_2 &= F_0 + (d - d_0)k_C - \varphi r k_C & \text{with } F_2 \geq 0, \end{aligned} \right\} \Rightarrow \left\{ \begin{aligned} F_C &= F_1 + F_2, \\ L_C &= (F_1 - F_2)r. \end{aligned} \right. \quad (18)$$

$F_1$  and  $F_2$  cannot be negative since they are caused by cables.

CCL1 is different to all other CCLs because of its relation of pulley radii: the radius of pulley1 is twice the radius of pulley2. Therefore, if the yoke rotates through an angle  $\beta$  with respect to the central body, panel1 rotates through  $2\beta$  with respect to the yoke, see Figure 8. If  $\beta = 90$  degrees the yoke and panel1 lie in one plane. With regards to the other CCLs, if panel2, panel4 and panel6 are kept parallel to the yoke and panel3 and panel5 are kept parallel to panel1, then all the bodies lie within one plane. In this position, the lock mechanisms are activated and fix one body with respect to its neighbours. As shown in Figure 8 the force laws for pulley2 of CCL1 are

$$\left\{ \begin{aligned} F_1 &= F_0 + (d - d_0)k_C + \varphi r k_C & \text{with } F_1 \geq 0, \\ F_2 &= F_0 + (d - d_0)k_C - \varphi r k_C & \text{with } F_2 \geq 0, \end{aligned} \right\}$$

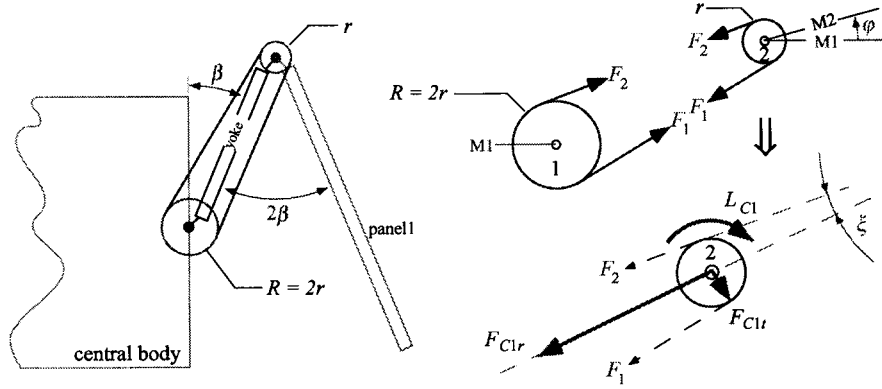


Figure 8. Forces and torques of CCL1 for stretched cables.

$$\Rightarrow \begin{cases} F_{C1r} = (F_1 + F_2) \cos \xi, \\ F_{C1t} = (F_1 - F_2) \sin \xi, \\ L_{C1} = (F_1 - F_2)r. \end{cases} \quad (19)$$

$F_1$  and  $F_2$  lead to the radial and tangential forces  $F_{C1r}$  and  $F_{C1t}$  and the torque  $L_{C1}$ . Equations (18) and (19) hold true for the following assumptions: (1) the cable forces  $F_1$  and  $F_2$  acting on a pulley always lie in the plane of the pulley and (2), two pulleys on one CCL are always parallel.

The *Motor-CCL* (MCCL) controls the rotation of the yoke with respect to the central body as shown in Figure 6. If the drive MCCL is locked, relative motion between all the panels and the yoke can only arise due to cable elasticity. Except for the cable elasticity, CCL1 to CCL6 avoid motions of panel1 to panel6 if the yoke rotation is locked. At the start of the array deployment, the MCCL is stationary prior to activating the release mechanisms, see Section 1. After transient oscillations have damped out the MCCL is activated and slowly rotates the yoke with respect to the central body until all the bodies are finally parallel and locked. At this time the MCCL is de-activated. The force laws for the two cable loops of the MCCL are equal to the force laws of the normal CCLs in (18). With  $\beta$  being the angle between the yoke and central body,  $\Omega$  the angular velocity of the motor, a ratio of radii 1 : 1,  $t_M$  the time when the Motor-CCL starts working,  $t$  the actual variable time, and  $t_0$  the initial time, the angle  $\varphi$  is given by

$$\begin{aligned} \varphi &= (\beta - \beta(t_0)) & \text{if } t < t_M, \\ \varphi &= (\beta - \beta(t_0)) + \Omega(t - t_M) & \text{if } t \geq t_M. \end{aligned} \quad (20)$$

Equations (16) to (20) are active referring to the deployment phases defined in Section 1.

#### 4. Mode Selection Using Modal Participation Factors

As mentioned in Section 2, eigenmodes and static modes to increase the convergence of the Ritz approximation are used to describe body deformations of multibody systems. For the yoke and panels, 30 eigenmodes (without rigid body modes) for three kinds of reference frames, as defined in Section 3, are prepared (Table I). Static modes may be included additionally. Of all these mode shapes, a proper set with a reasonable number of shapes is selected for the yoke and the panels and is inserted into the equations of motion. Since the modes are complex 3D shapes, an arbitrary selection based on the natural frequencies and their corresponding mode shapes is unlikely to be optimal. Therefore, the modal participation factor method is introduced as follows.

##### 4.1. MODAL PARTICIPATION FACTORS (MPF)

The deformation of a flexible body  $i$  with respect to the reference frame motion, given by  $\boldsymbol{\rho}^i$  and  $\boldsymbol{\alpha}^i$  is described by displacements  $\mathbf{u}^i(\mathbf{R}, t)$  and angles  $\boldsymbol{\vartheta}^i(\mathbf{R}, t)$ . They are written as a sum of assumed modes and time functions  $q_l^i(t)$ ,  $l = 1, \dots, n_q^i$ , as shown in (4) and (5). Thus, the position and orientation of a nodal frame at node  $k$  on body  $i$  with respect to the global frame are

$$\begin{aligned} \boldsymbol{\rho}^{k,i} &= \boldsymbol{\rho}^i + \mathbf{R}^{k,i} + \mathbf{u}^{k,i}(q_l^i), \quad \mathbf{A}^{k,i} = (\mathbf{E} - \tilde{\boldsymbol{\vartheta}}^{k,i}(q_l^i))\boldsymbol{\Gamma}^{k,i}\mathbf{A}^i(\boldsymbol{\alpha}^i), \quad \text{where} \\ \mathbf{u}^{k,i} &= [u_{\alpha}^{k,i}], \quad u_{\alpha}^{k,i} = \sum_{l=1}^{n_q^i} \Phi_{\alpha l}^{k,i} q_l^i, \quad \boldsymbol{\vartheta}^{k,i} = [\vartheta_{\alpha}^{k,i}], \quad \vartheta_{\alpha}^{k,i} = \sum_{l=1}^{n_q^i} \Psi_{\alpha l}^{k,i} q_l^i. \end{aligned} \quad (21)$$

If  $\mathbf{u}^{k,i}$  and  $\boldsymbol{\vartheta}^{k,i}$  are the correct solution (or an approximation), the relative contribution of  $q_l^i$  in the deformation is given as

$$\begin{aligned} P_{ul} &= |u_{\alpha l}^{k,i} / u_{\alpha}^{k,i}| = |\Phi_{\alpha l}^{k,i} q_l^i / u_{\alpha}^{k,i}| \quad \text{and} \\ P_{\vartheta l} &= |\vartheta_{\alpha l}^{k,i} / \vartheta_{\alpha}^{k,i}| = |\Psi_{\alpha l}^{k,i} q_l^i / \vartheta_{\alpha}^{k,i}|, \end{aligned} \quad (22)$$

where Equation (22) defines the so-called modal participation factors (MPF) of translational and rotational deformations. Calculation of the ratio  $P_{ql} = |q_l / q_{l\max}|$  is only allowed if all shape functions are normalised (e.g. if the modal mass matrix  $\mathbf{M}_e^i$  is an identity matrix).

For computation of (22), an estimation of is proposed solving a quasi-static configuration of the body  $i$  due to a specific load case. The loads are estimated or obtained by a rigid body simulation. Assuming that  $\mathbf{M}_e^i \ddot{\mathbf{q}}^i + \mathbf{D}_e^i \dot{\mathbf{q}}^i + \mathbf{K}_e^i \mathbf{q}^i \ll \mathbf{K}_e^i \mathbf{q}^i$  and neglecting gyroscopic and geometric stiffening terms, (12), (13) and (6) yields for body  $i$

$$\mathbf{K}_e^i \mathbf{q}^i - \mathbf{G}_e^{iT} \boldsymbol{\lambda} = \underbrace{-\mathbf{C}_t^i(\dot{\mathbf{v}}^i + \tilde{\boldsymbol{\omega}}^i \mathbf{v}^i - \mathbf{g}^i) - \mathbf{C}_{r0}^i \dot{\boldsymbol{\omega}}^i - \mathbf{O}_{e0}^i \boldsymbol{\omega}_q^i}_{\text{known inertia forces}}$$



$$+ \underbrace{\sum_k (\Phi^{k,i^T} \mathbf{F}^{k,i} + \Psi^{k,i^T} \mathbf{L}^{k,i})}_{\text{known nodal forces}}. \quad (23)$$

$$\mathbf{g}(\mathbf{z}_I(\mathbf{q}^i) = \mathbf{0} \quad \text{and} \quad \mathbf{G}_e^i = \partial \mathbf{g} / \partial \mathbf{q}^i. \quad (24)$$

In (23),  $\mathbf{K}_e^i$  is the generalised stiffness matrix,  $\mathbf{C}_t^i$  and  $\mathbf{C}_{r0}^i$  are matrices given by (9),  $\dot{\mathbf{v}}^i$ ,  $\dot{\boldsymbol{\omega}}^i$ ,  $\mathbf{v}^i$  and  $\boldsymbol{\omega}^i$  are accelerations and velocities of the reference frame (3),  $\mathbf{g}^i$  is the gravitational acceleration,  $\boldsymbol{\omega}_q^i$  is a  $6 \times 1$  matrix of products of  $\boldsymbol{\omega}^i$  and  $\mathbf{O}_{e0}^i$  a matrix of mass integrals representing centrifugal forces [16]. The sum of these terms represents inertia forces.  $\mathbf{F}^{k,i}$  and  $\mathbf{L}^{k,i}$  are applied forces and torques at nodes  $k, i$ , which are summarised for all nodes  $k$  of body  $i$ . If the shape function  $\Phi^i$  and  $\Psi^i$  satisfy the kinematical conditions *a priori*,  $\mathbf{g}$  in (24) is independent of  $\mathbf{q}^i$ ,  $\mathbf{G}_e^i$  equals zero and the static equilibrium Equation (23) are independent of constraint forces  $\boldsymbol{\lambda}$ .

Defining  $\dot{\mathbf{v}}^i$ ,  $\dot{\boldsymbol{\omega}}^i$ ,  $\mathbf{v}^i$ ,  $\boldsymbol{\omega}_q^i$ ,  $\mathbf{F}^{k,i}$ ,  $\mathbf{L}^{k,i}$  and  $\boldsymbol{\lambda}$  as given quasi-static loads, the deformation variables  $\mathbf{q}^i = [q_l^i]$  are obtained by solving the linear equations (23) together with (24), thus allowing for evaluation of the participation factors  $P_{ul}$ ,  $P_{\vartheta l}$  and  $P_{ql}$  in (22).

#### 4.2. EXAMPLES OF SIMPLE BEAM

The first example demonstrates the approximation of the deformation of a cantilever beam with a torque  $L^B$  at the tip (Figure 9a). The beam is modelled as a flexible body  $i = 1$  with a tangent frame and natural modes of the cantilever beam (Figure 9b). From geometrical and material data, the matrices in (23),  $\mathbf{K}_e^i$ ,  $\mathbf{G}_e^i = \mathbf{0}$ ,  $\Phi^A$ ,  $\Phi^B$ ,  $\Psi^A$  and  $\Psi^B$  at nodes  $A$  and  $B$  are calculated, yielding  $\mathbf{q}^i$  and the deformations at the tip given by  $\mathbf{u}^{k,i}$  and  $\boldsymbol{\vartheta}^{k,i}$ . Here  $\boldsymbol{\rho}^i$  and  $\boldsymbol{\alpha}^i$  zero. The MPF for a configuration as given in Figure 9a are plotted in Figure 9c. It shows that the share of the modes higher than four is less than 1% for displacement  $y^B$ , but for the slope  $\alpha^B$ , all modes are required to have an error of less than 1% with respect to the analytical solution given in Figure 9a.

In a second example we consider a rotating beam in a quasi-static equilibrium with loads  $F^B = -2$  N and  $L^B = 3$  Nm (Figure 10a). This problem is to be solved with a flexible body  $i$  attached to a revolute joint and using a Buckens frame with natural modes of an unsupported beam (Figure 10b). Inserting the given data into (23), (24) and (22) yields MPF as shown in Figure 10c. Here, the constraint forces  $\boldsymbol{\lambda}$  at the hinge (point  $A$ ) are taken into account, and are non-zero. As the MPF in Figure 10c prove, the deformation of the beam with respect to the body frame requires all eight modes achieving an error of less than 1%. As in the previous example, the slope is more sensitive. Additional errors arise when using mode shapes of a finite element approximation based on variation of number and types of elements. This is not discussed here.

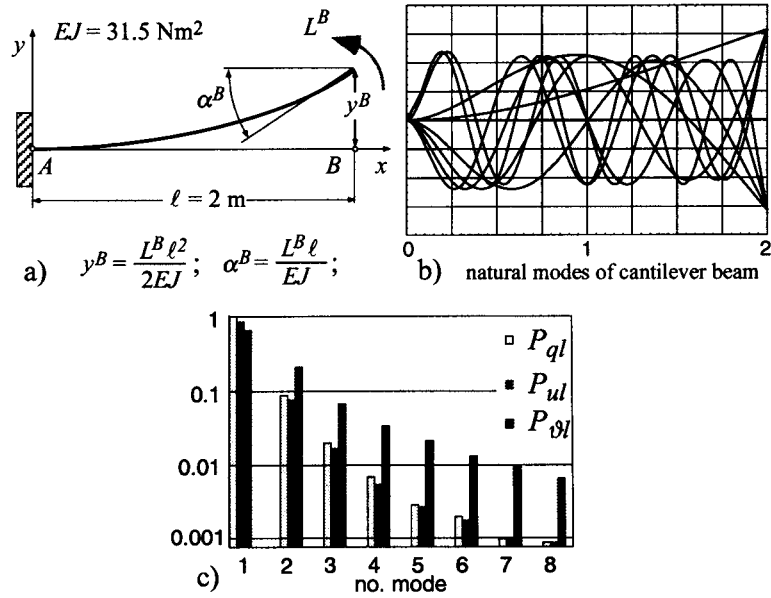


Figure 9. Modal participation factors when approximating the static deflection of a cantilever beam with its natural modes. (a) Static problem, (b) mode shapes of cantilever beam, (c) MPF on solution of (a).

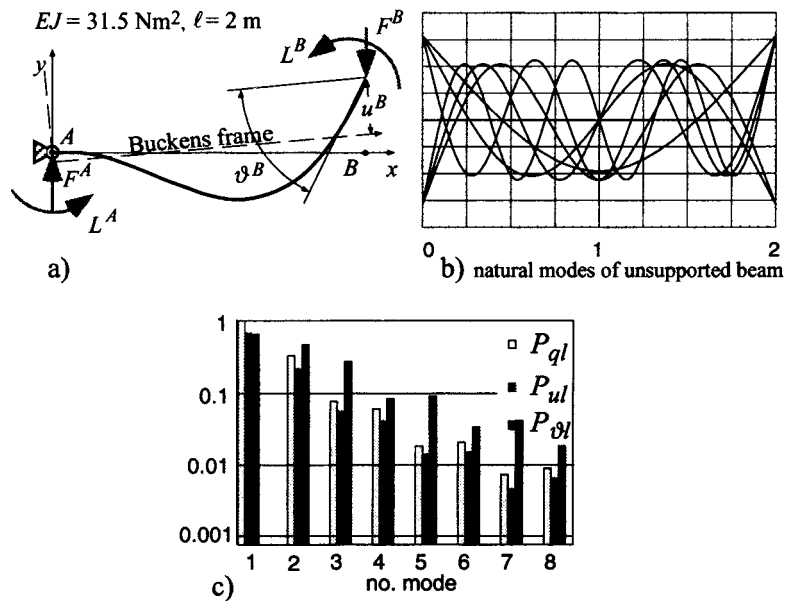


Figure 10. Modal participation factors when approximating the static deflection of a rotating beam with exact free-free modes. (a) static problem, (b) mode shapes of free-free beam, (c) MPF on solution of (a).

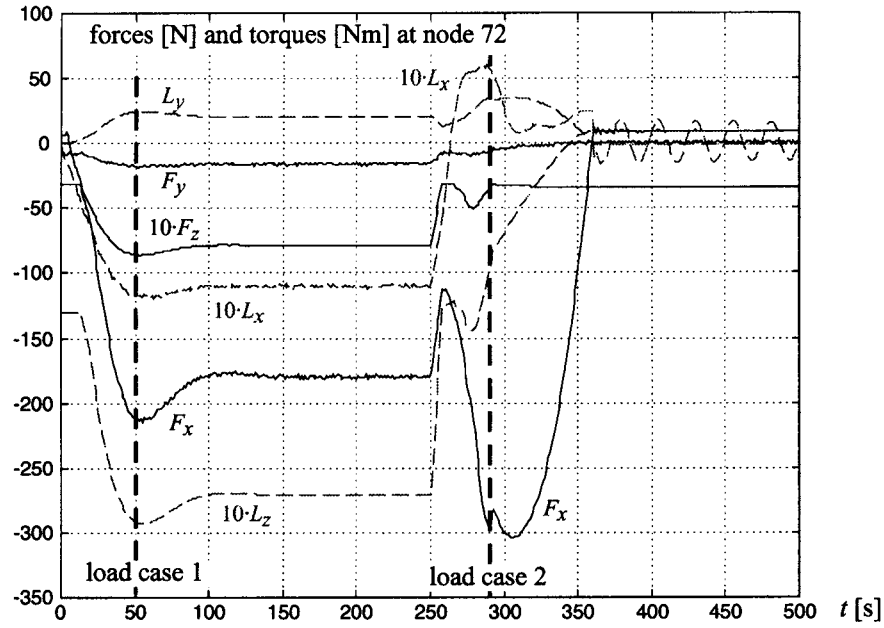


Figure 11. Results of the deployment of a solar array using the rigid body model.

#### 4.3. MODAL PARTICIPATION FACTORS FOR THE YOKE

The yoke is a flexible body supported by hinges at the satellite side (at nodes 172, 173) and the panel side (node 71, 72; see Figure 5). As listed in Table I, 30 natural modes for three kinds of reference frames are prepared. To select a reduced set of modes, the participation factor method for the frame case (2) – Buckens frame rotating at hinges at node 172, 173 with mode shapes of a rotating structure – is applied.

During the deployment of the solar array, the loads required in (23) are estimated using a rigid body model. For example, Figure 11 shows the nodal forces and torques at node 72. Taking the load cases at time  $t = 50$  sec and  $t = 290$  sec, from (22) and (23) we obtain the MPF  $P_{ql}$  as well as  $P_{ul}$  and  $P_{\vartheta l}$  for all nodes of interest. Figure 12 (left side) shows  $P_{ql}$  and the influence on the deformation at nodes 71 and 72. Modes with factors smaller than 1% are neglected. The remaining dominant mode shapes for the yoke are listed in (25). Figure 12 (right side) shows that the eigenmodes do not converge continuously; modes 21 and 27 have a bigger share in the solution than the previous modes.

$$\text{Mode shape numbers for the yoke: } 1, 2, 3, 4, 5, 6, 7, 8, 9, 10, 13, 18, 21, 25, 27. \quad (25)$$

The computation of MPF for other load cases and nodal displacements allows for the selection of a set of mode shapes that satisfy all the various load cases (i.e. selecting the mode shapes in a quasi-optimal fashion). Static modes can also be

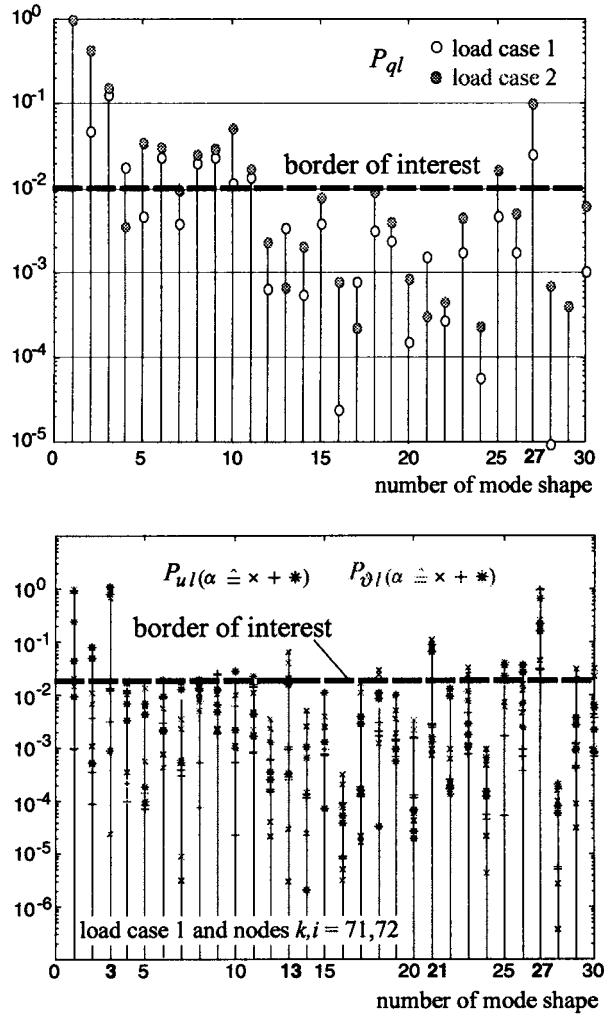


Figure 12. Modal participation factors for mode shapes of the rotating yoke structure.

taken into account. In a similar way, the shape functions of the panels are chosen and marked by  $\bullet$  in Table I.

## 5. Simulation Results of Deployment the Solar Array

Based on the descriptions of the bodies, joints and deployment mechanisms in Section 3 and the mode selection in Section 4, the deployment is simulated for various models of bodies [20]. Four models are discussed below:

- (I) All bodies are **rigid**, thus  $n_z = 56$  and  $n_{DAE} = 161$ , see (15).

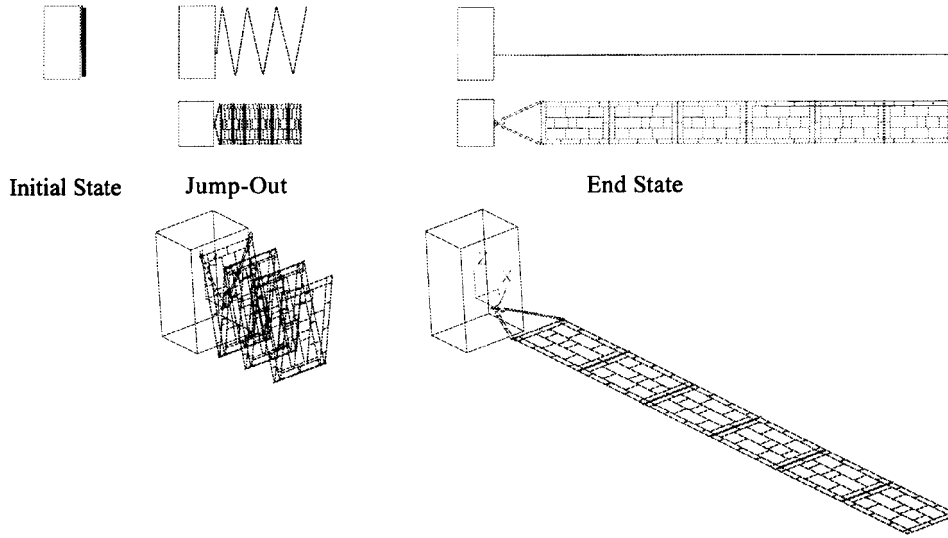


Figure 13. Motion of the solar array during the deployment.

- (II) The yoke and panels are flexible. The flexibility of the yoke is represented by 15 eigenmodes of mode set (2) – the **rotating structure**, see (25). For the panels, eight eigenmodes of mode set (2) are used, see Table I. Here,  $n_z = 119$  and  $n_{DAE} = 287$ .
- (III) The yoke and panels are flexible as in (II) described by 15 and eight eigenmodes, respectively, but the modes are taken from **unsupported structures**, case 1 in Table I.
- (IV) As in (II) but the modes shapes of the yoke and the panels are obtained by the **simple supported structures**, see case 3 in Table I.

The CPU time is 189 sec for the rigid model (I), 4287 sec for model (II) and 4857 sec for model (III). Figure 13 shows the deployment of the solar array as defined in Section 1. The deployment begins with the jump-out phase with the yoke and panels completely folded and lasts 250 sec. Then the Motor-CCL is activated and rotates the yoke as defined by (20) – steering phase. After about 360 sec, the panels are locked and the Motor-CCL is stopped. The deployed configuration is reached. For 140 sec or more, the panels keep oscillating with small amplitudes. The natural damping of the structure is assumed to be 2%.

In Figure 14, the torques of CCL1, CCL6, and of one of the Motor-CCLs are shown for the rigid model (I) and the flexible model (II). At the end of the jump-out phase the corrective torque  $L_C$  of CCL6 is exactly  $-2$  Nm caused by the two deployment springs at panel6. Since one CCL passes on its corrective torque  $L_C$  to the following via the bodies it connects, CCL1 has to compensate 12 Nm ( $= 6 \cdot 2$  Nm) at pulley2 and, due to the relation of the radii, 24 Nm at pulley1 (Figure 8). The two Motor-CCLs have to compensate 12 Nm of CCL1, plus the torque resulting from

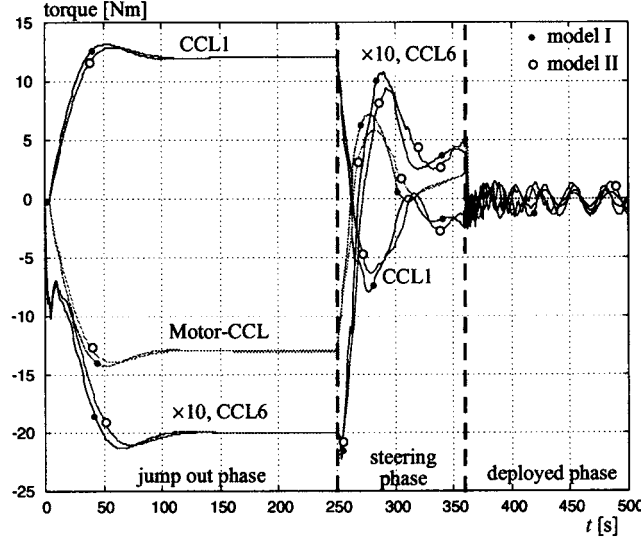


Figure 14. Results of time history of the deployment for the rigid model (I) and flexible model (II).

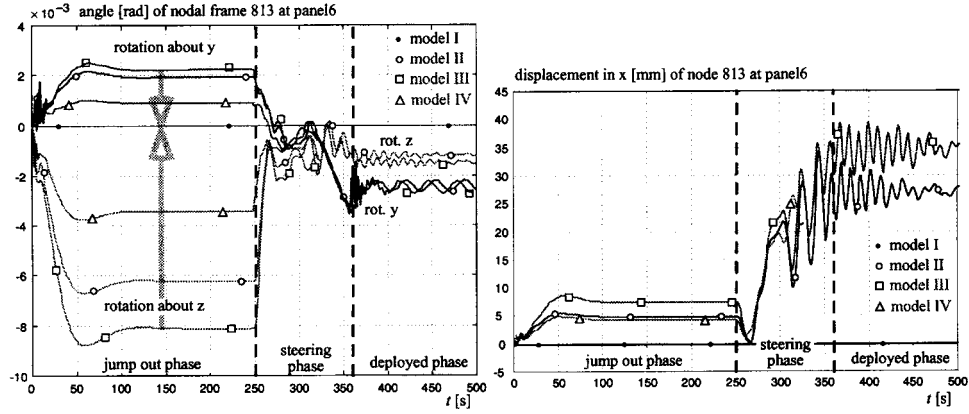


Figure 15. Results of time history of the deployment for the rigid model (I) and flexible models (II), (III), and (IV).

$F_{Clt}$  given in (19) times the length of the yoke plus 2 Nm of the yoke deployment springs. Since times the length of the yoke is also exactly 12 Nm, each of the two Motor-CCLs has to compensate 13 Nm.

A comparison of models (I) and (II) shows that the torques decrease only by about 2% during the jump-out phase if the bodies are flexible, and by 21% during the steering phase. The oscillation in the deployed configuration is almost identical for both models. Differences between models (I) and (II) are small.

In Figure 15 (left side) the absolute angles  $\alpha_y^{k,i}$  and  $\alpha_z^{k,i}$  at node  $k, i = 813$  of panel6 are plotted. For model (I), the angles are zero. In the flexible models,

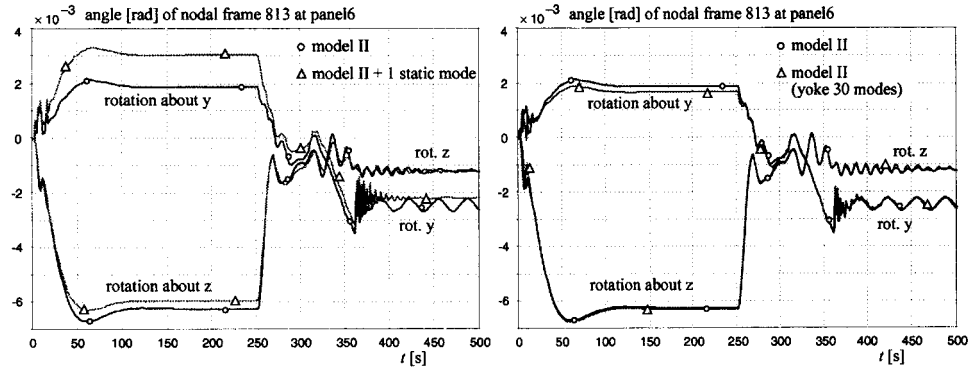


Figure 16. Results of time history of the deployment for variations numbers of mode shapes.

panel6 rotates about the  $y$ - and  $z$ -axis. In the deployed configuration, panel6 has a steady state value of  $\alpha_v^{k,i} = 0.002$  rad leading displacements at node 574 and 913 (Figure 5). Compared to the rigid model (I), the elastic deviation in the  $z$ -direction is  $-2.7$  mm and  $+2.7$  mm at nodes 574 and 913, respectively.

Figure 15 (right side) shows the displacement in  $x$ -direction at node 813 of panel6. As mentioned before, the corresponding rigid body model value is zero, whereas the flexible models yield steady state deformations of about 30 mm after the deployment. Figure 15 proves that the differences between model (II) and (III) or (IV) are significant for rotations and a structure described by mode shapes with stiffer boundary conditions decreases the amplitudes.

Figure 16 (left side) shows the influence of the static modes on the results. The only difference between the models is one additional static mode for the yoke and for each of the panels. As can be seen, one additional static mode for each flexible body can change the results significantly, even if the number of mode shapes is already relatively high.

Figure 16 (right side) illustrates the effect of increasing the number of mode shapes for the yoke from 15 to 30. The number of mode shapes for the panels is 8 in both models. The figure demonstrates the efficiency of a mode shape selection using the participation factor method: For 15 additional mode shapes (i.e. an increase of 100% in the number of mode shapes) of the yoke, the results change only slightly, although the flexibility of the yoke is the most dominant factor in the simulations.

In [20], more models are analysed for other sets of mode shapes and integrator settings and also for various static modes. The simulation results of those models are similar to the results presented here.

The static offsets after deployment in Figures 15 and 16 are due to the deployment springs always being active and thus working against the lock mechanisms, and also due to the asymmetric pulley mechanisms in connection with the inclined yoke and panel appendages (Figure 1). These appendages allow for offset hinge

lines so that the yoke and panels can be folded perfectly parallel without gaps before deployment, see Figure 13 (initial state).

Hence the deployment springs cause static rotational offsets of the yoke and panels (also in the rigid body model), and the pulley mechanisms in connection with the appendages excite torsional modes during and after deployment in the flexible body models.

## 6. Conclusion

The deployment of a satellite solar array is simulated using the multibody program SIMPACK. A rigid body model (I) is compared with three flexible models (II), (III) and (IV), applying various sets of shape functions. The deployment mechanisms are implemented in detail for the three phases of deployment: jump-out phase, steering phase and deployed phase.

The flexibility of the yoke and panels is represented by a set of natural modes and some static modes obtained by a finite element analysis. In order to reduce the computational burden a modal participation factor method is applied to select the significant modes. The factors of each mode as shown in Figure 12 are computed solving a quasi-static equilibrium of the flexible body, and the loads are obtained by a rigid body simulation. A simulation with the full set of modes (Figure 16) demonstrates the power of the method.

The comparison of the results of the rigid body model (I) with the flexible body models (II), (III) and (IV) shows that flexible bodies cause a slightly changed torque in the closed cable mechanisms. The steady state rotations and the deflection in  $x$ -direction of the panels are only occur for the flexible models, and the rotations about the  $y$ -axis are caused by deformations of the panels, whereas rotations about the  $z$ -axis are caused by the flexibility of the yoke. The solar generator is relatively stiff and the magnitudes of deformation are therefore relatively small. The differences of the deformations between the flexible models (II), (III) and (IV) are significant and need further research in the usage of the multibody program SIMPACK.

## Acknowledgements

The authors wish to express their thanks to the DaimlerChrysler Aerospace, Otto-brunn, Germany, for providing the model and parameters of the solar array, and for supporting the project.

## References

1. Bremer, H. and Pfeiffer, F., *Elastische Mehrkörpersysteme*, Teubner Studienbücher, Mechanik, Teubner, B.G., Stuttgart, 1992.
2. Dietz, S., *Vibration and Fatigue Analysis of Vehicle Systems Using Component Modes*, Fortschr. Berichte VDI, Reihe 12, Nr. 401, VDI-Verlag, Düsseldorf, 1999.



3. Eich-Soellner, E. and Führer, C., *Numerical Methods in Multibody Dynamics*, Teubner-Verlag, Stuttgart, 1998.
4. Hagedorn, P., 'The Rayleigh–Ritz method with quasi-comparison functions in nonself-adjoint problems', *Journal of Vibration and Acoustics* **115**, 1993, 280–284.
5. Meirovitch, L. and Hagedorn, P., 'A new approach to the modelling of distributed non-self-adjointed systems', *Journal of Sound and Vibration* **178**(2), 1994, 227–241.
6. Meirovitch, L. and Kwak, M.K., 'Convergence of the classical Rayleigh–Ritz method and the finite element method', *AIAA Journal* **28**(8), 1990, 1509–1516.
7. Otter, M., Hocke, M., Daberkow, A. and Leister, G., 'An object oriented data model for multibody systems', in *Proceedings of the International Symposium on Advanced Multibody System Dynamics*, W. Schiehlen (ed.), Kluwer Academic Publishers, Dordrecht, 1993, 19–48.
8. Roberson, R.E. and Schwertassek, R., *Dynamics of Multibody Systems*, Springer-Verlag, Berlin, 1988.
9. Rulka, W., 'SIMPACK, A computer program for simulations of large-motion multibody systems', in *Multibody System Handbook*, W. Schiehlen (ed.), Springer-Verlag, Berlin, 1990, 265–284.
10. Schwertassek, R., 'Flexible bodies in multibody systems', in *Computational Methods in Mechanical Systems*, J. Angeles and E. Zakhariyev (eds), Springer-Verlag, Berlin, 1997, 329–363.
11. Schwertassek, R. and Wallrapp, O., *Dynamik flexibler Mehrkörpersysteme*, Vieweg Verlag, Braunschweig, 1999.
12. Shabana, A.A., 'Resonance conditions and deformable body coordinate systems', *Journal of Sound and Vibration* **192**(1), 1996, 389–398.
13. Shabana, A.A., 'Flexible multibody dynamics: Review of past and recent developments', *Multibody System Dynamics* **1**, 1997, 189–222.
14. Spanos, J.T. and Tsuha, W.S., 'Selection of component modes for flexible multibody simulation', *Journal of Guidance* **14**(2), 1991, 278–286.
15. Verlinden, O., 'Simulation du comportement dynamique de systemes multicorps flexibles comportant des membrures de forme complexe', Ph.D. Thesis, Faculté Polytechnique de Mons, 1994.
16. Wallrapp, O., 'Standard input data of flexible members for multibody system codes', in *Advanced Multibody System Dynamics – Simulation and Software Tools*, W. Schiehlen (ed.), Kluwer Academic Publishers, Dordrecht, 1993, 445–450.
17. Wallrapp, O., *Beam – A Pre-Processor for Mode Shape Analysis of Straight Beam Structures and Generation of the SID File for MBS Codes, User's Manual*, Deutsche Forschungsanstalt für Luft- und Raumfahrt (DLR), Inst. Robotik und Systemdynamik, Oberpfaffenhofen, Report Version 3.0, 1994.
18. Wallrapp, O., 'Standardization of flexible body modeling in multibody system codes, Part I: Definition of standard input data', *Mechanics of Structures and Machines* **22**(3), 1994, 283–304.
19. Wallrapp, O., Eichberger, A. and Gerl, J., *FEMBS – An Interface between FEM Codes and MBS Codes, User Manual for ANSYS, NASTRAN, and ABAQUS*, INTEC GmbH, Wessling, Report Version 3.0, 1997.
20. Wiedemann, S., 'Entfaltanalyse Solargenerator unter Berücksichtigung von Elastizitäten mit SIMPACK', Diplomarbeit, Fachhochschule München – Munich University of Applied Sciences, 1999.